Research Article | Vol. 28, No. 8 / 13 April 2020 / Optics Express 11128
Optics EXPRESS

Electrodynamic simulation of laser beam propagation in waterjet-guided laser processing

CHUN DENG, HARAM YEO, AND HYUNGSON KI*

Department of Mechanical Engineering, Ulsan National Institute of Science and Technology (UNIST), 50 UNIST-gil, Ulsan 44919, South Korea
*hski@unist.ac.kr

Abstract: Waterjet-guided material processing is a technique that combines the capabilities of laser material processing with water jetting. In this study, we have investigated laser beam propagation in a waterjet column by numerically solving the Maxwell equations and the heat equation. A 1064 nm laser and its frequency-doubled 532 nm laser were chosen for the simulations, and the finite-difference time-domain (FDTD) method was employed for solving the Maxwell equations. The coupling effect of the laser and waterjet was simulated with different numerical apertures and different waterjet column diameters. Extensive investigations on laser absorption phenomena regarding the outer surface geometries of the waterjet (cylindrical shape with and without sinusoidal perturbation), and temperature distributions were also conducted. To the best of the authors' knowledge, this is the first electrodynamic simulation of laser beam propagation and interaction with a water column in waterjet-guided laser processing. Some interesting findings concerning laser beam absorption characteristics inside a waterjet column were revealed.

1. Introduction

Waterjet-guided laser processing is a technique that was initially proposed in 1993 by scientists at the Institute for Applied Optics from Lausanne University of Technology in Switzerland. They successfully guided the laser beam with a pressurized waterjet, named Microjet by the inventors, onto the workpiece surface for fabrication. Because of the different refractive indices of air and water, the laser beam undergoes total internal reflection at the transition zone between the water and air media, in a manner similar to conventional optical glass fibers [1–3]. The laser beam is confined inside the waterjet column and concentrated energy is delivered through the waterjet without much divergence, making the process efficient and viable over a large working distance. The pressurized waterjet also works as a cooling medium to remove the heat and the debris that is generated from the laser processing [4–6]. This ensures shallow thermal penetration, clean cuts, and the avoidance of deviations in tolerance [7].

The laser beam is focused into a nozzle by a lens, after which step the beam is coupled with a pressurized water chamber [8]. The geometries of the chamber and nozzle are of great importance in coupling the energy-rich laser beam into the low-pressure waterjet column [9]. The hair-thin low-pressure cylindrical waterjet that is emitted from the nozzle, confines and guides the laser beam parallel to its axis through total internal reflection at the water/air interface. This ensures a more constant "processing beam size" and uniform energy distribution at the point of interaction when compared to that of conventional laser material processing. The uniformly distributed laser intensity leads to a higher quality and smoother cuts that are free from cracking and chipping. The variable length of a stable waterjet also eliminates the need for optical focus control, allowing precision machining to a considerable depth. This technique has been applied to cut a large variety of materials, especially in the treatment of heat sensitive materials (biomedical devices) as well as in high precision products, such as solar cells, wafer dicing, electronics, etc.

Limited work has been done in terms of studying the process of waterjet assisted laser processing. Li et al. [10] have simulated the heat transfer for waterjet assisted silicon drilling

#389497 https://doi.org/10.1364/OE.389497
Journal © 2020 Received 30 Jan 2020; revised 14 Mar 2020; accepted 14 Mar 2020; published 31 Mar 2020

Optics EXPRESS

with a finite difference method. Their results show the thermal field and phase changes involved during the cutting process. Kray et al. [11] have studied the edge isolation of industrial silicon solar cells with a waterjet-guided laser. A great potential to improve the laser scribing process in terms of pn junction damage and mechanical stability has been demonstrated with their work. Shi et al. [7] fabricated functional surfaces by waterjet guided micro machining. Stable superhydrophobic properties were achieved on stainless steel surfaces. Marimuthu et al. [12] adopted the waterjet guided laser processing for the drilling of SiC reinforced aluminium metal matrix composites with exceptional quality. Sun et al. [13] experimentally investigated the waterjet guided laser processing for carbon fiber reinforced plastics (CFRP) cutting for the first time and some promising results were reported. However, most of the previous work has only focused on the interaction between the laser and the workpiece, while investigations on how laser beams propagate inside the waterjets were rarely discussed. The viability and fabrication quality of the waterjet-guided fabrication strongly rely on how and how much laser energy is delivered through the waterjet to the workpiece. Therefore, accurate predictions of laser beam propagation and laser beam absorption inside the waterjet column are arguably some of the most important but challenging tasks in the study of waterjet-guided laser processing.

In this study, laser propagation within a fully developed waterjet column was investigated by solving the Maxwell equations using the finite-difference time-domain (FDTD) method combined with an wavelength enlargement algorithm [14]. A laser beam is an electromagnetic (EM) wave in nature, and the electromagnetic characteristics, such as focusing, absorption, reflection, and refraction, can be naturally taken into account with full electrodynamic simulations. Recently, the FDTD algorithm for electrodynamic simulations has drawn a lot of attention because it can be utilized to solve the Maxwell equations directly [15]. The biggest challenge to the use of this algorithm is, however, that because the laser wavelength is extremely small when compared to the simulation domain size for a typical laser manufacturing problem, a very high grid density is required for the calculations, especially for three dimensional simulations. In order to resolve this issue, Deng and Ki [14] reported a numerical algorithm for increasing the laser beam wavelength while preserving the laser absorption characteristics. In this manner, the grid requirement can be reduced significantly [14,16,17]. In this study, a 1064 nm laser and its frequency-doubled 532 nm laser were chosen for the simulations. An extensive investigation on laser/waterjet coupling, laser absorption phenomena considering the outer surface geometries of the waterjet (periods/amplitude of the wavy surface), Joule heating effects, and possible temperature distribution inside the waterjet were conducted with circularly polarized Gaussian beams.

2. Mathematical model

A typical waterjet-guided laser processing technique is schematically shown in Fig. 1.

To simulate the laser beam propagation within a waterjet column and its propagation inside the waterjet through total internal reflection, an FDTD algorithm was adopted. FDTD is an algorithm for accurately solving the Maxwell equations that are expressed as,

$$\nabla \cdot (\tilde{\varepsilon}\mathbf{E}) = \rho_f \tag{1}$$

$$\nabla \cdot (\mu\mathbf{H}) = 0 \tag{2}$$

$$\nabla \times \mathbf{E} = -\frac{\partial(\mu\mathbf{H})}{\partial t} \tag{3}$$

$$\nabla \times \mathbf{H} = \frac{\partial(\tilde{\varepsilon}\mathbf{E})}{\partial t} + \mathbf{J} \tag{4}$$

where $\tilde{\varepsilon}$ and μ are the complex permittivity and permeability of the medium, ρ_f and J are the free charge density and current density, and $\mathbf{E}$ and $\mathbf{H}$ are the electric field and magnetic field in

Optics EXPRESS

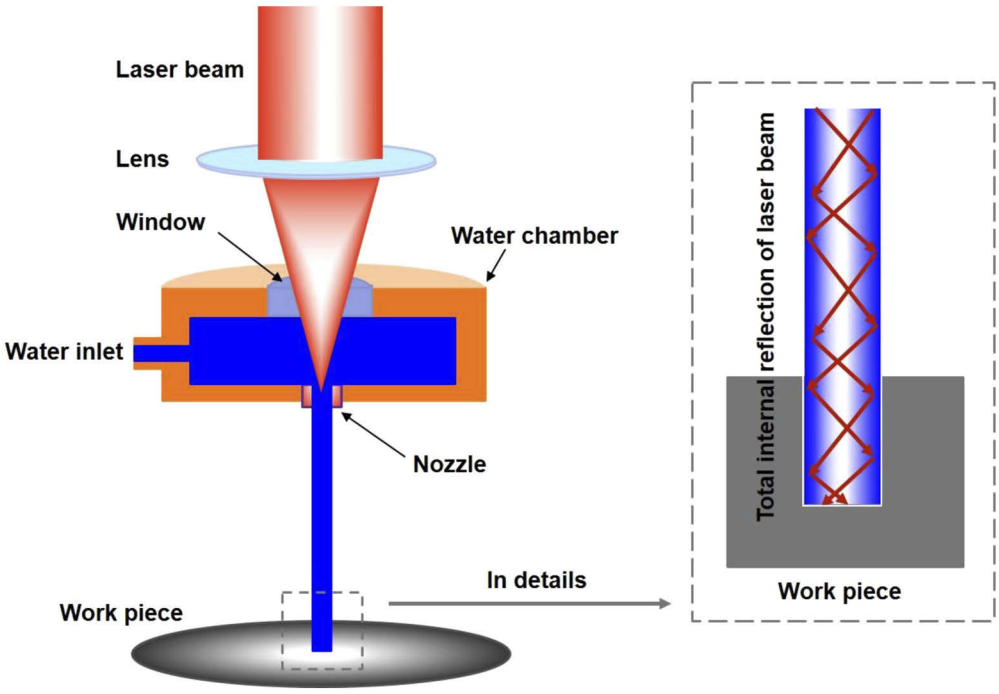

Fig. 1. Schematic of a standard waterjet-guided laser processing setup.

the domain, respectively. The FDTD method falls into the general class of grid-based differential numerical modeling methods. The time-dependent Maxwell's equations are discretized using central-difference approximations to the space and time partial derivatives. The resulting finite-difference equations are solved in a leapfrog manner until the desired transient or steady-state electromagnetic field behavior is fully evolved.

A Gaussian beam was assumed and was implemented in terms of the electric field. For instance, the components (in x and y directions) of a circularly polarized laser beam are mathematically expressed as

$$E_{x,y}(x, y, z) = E_0 \exp\left(\frac{-(x^2 + y^2)}{r_0^2}\right) \sin(\omega t), \tag{5}$$

where E_0 is the electric field at the center of the beam profile, r_0 is beam radius, $-z$ is the laser beam propagation direction, and ω is the laser beam angular frequency.

When selecting a laser for the waterjet-guided laser processing, laser wavelength is the key factor because the absorption coefficient of water widely changes with the wavelength. The absorption coefficient of water for a wide wavelength range is well documented in many reference [18–20]. In the ultraviolet wavelength range, the absorption coefficient is very large (e.g., 0.1 cm^{-1} for 193 nm), and it decreases as the wavelength increases. At ~450 nm, it reaches the minimum and then increases again toward the infrared wavelength region. The maximum occurs at around 2.94 μm (which is the wavelength of the Er:YAG laser), where the absorption coefficient is 12000 μm. This absorption characteristic of water clearly indicates that at ~450 nm, the water absorption (and energy loss) is minimum while at wavelengths larger than 450 nm the absorption will be much higher. In this study, a 1064 nm laser beam and its frequency-doubled 532 nm laser beam were chosen for the simulations for the sake of comparison. As well known, a 1064 nm laser is cheaper, and it is preferred in the industry; however, it has a much higher

Optics EXPRESS

absorption in water. On the other hand, a 532 nm wavelength laser (which is fairly close to 450 nm) is more expensive but reasonably transparent in water, ensuring a much higher energy output. The absorption coefficients of water are 0.00035 cm^{-1} for 532 nm and 0.61 cm^{-1} for 1064 nm. Moreover, if another working liquid (other than water) is selected, one can refer to its respective absorption spectrum for guidance, ensuring a low energy loss wavelength for the process.

In this study, the laser beams were focused at the top surface of the waterjet that was emitted from the pressurized water chamber (usually at a pressure ranging from 20 bar to 500 bar) through a nozzle. For conventional "dry" laser processing, the working laser beam normally has a conical shape after focusing due to the beam divergence. With the waterjet-guided laser, however, which can be classified as a "cold" laser, the laser beam is confined within the thin waterjet through total internal reflection, and it is guided onto the workpiece surface for processing. The absence of a focal point for the concentrated beam and the cooling/removing effects of the waterjet provide a long working distance, small heat affected zone (HAZ), clean kerfs, and straight cuts.

The waterjet is usually modeled as a cylindrical column for simplicity; for accurate predictions however, the waterjet column instability needs to be taken into consideration. Liquid jets become unstable and break up into a series of small droplets after a certain length due to the Plateau-Rayleigh instability under most circumstances [21,22], because of the liquid surface tension. The deformation of a liquid column, also generally known as varicose perturbation, is depicted as a series of periodic displacement sinusoids, as shown in Fig. 2. The working length of the water column for waterjet-guided laser processing is usually in the range of several centimeters (depends on the waterjet pressure), and the velocity of the laser beam propagating inside the waterjet is much larger than the velocity of the emitted waterjet. Therefore, the waterjet can be considered stationary for the FDTD simulations. To limit the thermal effects on the workpiece during cutting, the pulse duration of the laser beam normally lasts fewer than 10 ns. However, in the FDTD simulations, we only focus on the laser beam propagation inside the waterjet column, while the interaction between the laser beam and the workpiece will not be considered.

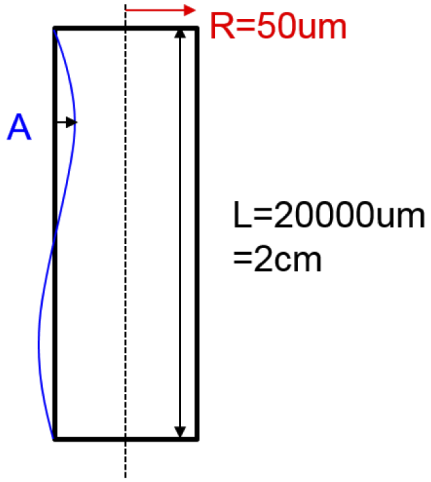

Fig. 2. Cylindrical shaped (Black) and a single sinusoidal shaped (Blue) waterjet column are presented here as an example.

A three-dimensional domain of 150 μm × 150 μm × 2 cm was used with a grid size of $\Delta x_{FDTD} = \Delta y_{FDTD} = \Delta z_{FDTD} = \frac{\lambda}{(10\times n)}$, where λ is the laser wavelength and n is the refractive index of the medium, respectively. A special absorbing boundary condition had to be applied to truncate the computational domain as well as to eliminate the artificially-reflected-back

Optics EXPRESS

electromagnetic waves at the boundary. In this study, the convolutional perfectly matched layer (CPML) absorbing boundary condition was employed, which is accurate, efficient, and suited for domains with generalized materials [23]. By using the defined computational domain and FDTD algorithm, laser propagation patterns, laser energy transmission inside the waterjet, and Joule heating patterns can be obtained. The energy transmission value T of the waterjet through simulation is calculated using the following equation,

$$T = \frac{\int |\mathbf{n} \cdot (\mathbf{E} \times \mathbf{H})| dA_{bottom}}{\int |\mathbf{n} \cdot (\mathbf{E} \times \mathbf{H})| dA_{incident}}, \tag{6}$$

where $\mathbf{n}$ is the unit normal vector at the surface where the Poynting vector is evaluated, A stands for a surface plane of the waterjet, and the subscripts *bottom* and *incident* denote the bottom surface plane of the waterjet and the incident surface plane at the top. The integrals in the numerator and denominator represent the energy flux passing through the bottom surface and the energy flux of the incident beam, respectively. In Table 1, the optical parameters of water at 532 and 1064 nm are given, together with the corresponding enlarged wavelength values calculated using the method presented in [14]. Note that the temperature dependency of optical properties was ignored in this study. The average laser power used for the simulations was 200 W.

Table 1. Parameters used for FDTD simulations with enlarged wavelengths for 532 nm and 1064 nm lasers.

Material	λ (nm)	n	κ	λ_{new} (μm)
Water	532	1.330	1.49×10^{-9}	5.89
Water	1064	1.326	5.13×10^{-6}	11.78

The Joule heating patterns were calculated by

$$J_h = \sigma_\lambda E^2, \tag{7}$$

where J_h is the Joule heating term and σ_λ is the electrical conductivity of water at a certain wavelength. Temperature distributions of the waterjet can then be calculated using the Joule heating term as the energy source in the energy equation as

$$\frac{\partial T}{\partial t} + \mathbf{u} \cdot \nabla T = \alpha \nabla^2 T + \frac{J_h}{\rho c_p}, \tag{8}$$

where T, $\mathbf{u}$, α, ρ and c_p denote temperature, velocity vector, thermal diffusivity, density, and constant-pressure specific heat, respectively. The material properties are expressed using the volume fraction law as

$$\begin{aligned} \alpha &= \alpha_a f_a + \alpha_w f_w \\ \rho &= \rho_a f_a + \rho_w f_w \\ c_p &= (c_p)_a f_a + (c_p)_w f_w \end{aligned}, \tag{9}$$

where f is the volume fraction and subscripts a and w denote air and water, respectively. Note that both the water column and the surrounding air were considered in the thermal simulation because the heat generated inside the water column can be transferred to the surrounding air. The properties used for the energy equation are shown in Table 2.

In this study, air was assumed stationary and water was assumed to flow downward with a constant speed U. The energy equation was discretized using the second-order central difference

Optics EXPRESS

Table 2. Properties used for the energy equation.

Material	α	ρ	c_p
Air	2.14×10^{-5} m^2/s	1.20 kg/m^3	1.01 kJ/kg K
Water	1.43×10^{-7} m^2/s	998.21 kg/m^3	4.18 kJ/kg K

in space and the first-order forward difference in time. In the energy equation, the following domain and grid sizes were used.

$$\begin{cases} L_{x,Energy} = 10L_{x,FDTD},\ L_{y,Energy} = 10L_{y,FDTD},\ L_{z,Energy} = L_{z,FDTD} \\ \Delta x_{Energy} = 4\Delta x_{FDTD},\ \Delta y_{Energy} = 4\Delta y_{FDTD},\ \Delta z_{Energy} = 10\Delta z_{FDTD} \end{cases} \tag{10}$$

Here, x and y represent lateral directions and z denotes the vertical direction, and L_x, L_y, L_z, Δx, Δy, and Δz are domain and grid sizes in the x, y, and z directions, respectively. For the time step, $\Delta t = \min(0.125\Delta x^2/\alpha, 0.500\Delta x/U)$ was used. In the thermal analysis, three waterjet speeds ($U = 0.1$ m/s, 2 m/s, 50 m/s) and two waterjet radii (R = 25 μm, 50 μm) were considered.

3. Results and discussion

Firstly, the laser/waterjet coupling effect was studied using combinations of different numerical aperture values of the system and different radii of the waterjet columns. The nozzles are generally made of sapphire or diamond, and their diameters vary between 25 and 100 μm [24]. A very small N.A. value of 0.1000 is normally used in laser cutting for smaller beam divergence, to ensure a straight cutting edge. With the presence of a waterjet to guide the laser beam, the laser is well confined and uniformly distributed within the waterjet, thereby a larger N.A value can be used. Here, to consider a wide range of N.A values for the waterjet guided laser processing, three numerical aperture values (large as 0.6650, half of the value of 0.6650, i.e., 0.3325 (moderate), and a small N.A. value as 0.1000) and three waterjet radii (25 μm, 50 μm and 100 μm) were used for both wavelengths. The results are shown in Fig. 3, Fig. 4, and Fig. 5, where white lines represent the water/air interfaces. Figures 3(a)–3(f) shows the results of N.A. = 0.6650 with two wavelengths and three types of waterjet radii. The leaked energy due to the coupling was calculated by the energy flux difference right above and below the waterjet entrance, and the values are shown as L in each figure in percentages. From Figs. 3(a)–3(c), where the waterjet radii varies from 25 to 50, and to 100 μm, the leakage is decreased from 0.605% to 0.118%, and finally to 0.024%. This is easily understood as a laser beam is more likely to escape from a smaller waterjet entrance than a larger one. The electric field inside a smaller waterjet column is much more intense due to the internal multi-reflections and interferences. The same conclusion can be drawn for Figs. 3(d)–3(f) with the doubled wavelength. The loss decreases (from 5.330% to 2.803%, and to 1.335%) with an increase in waterjet radii, and the electric fields are also more concentrated inside a smaller waterjet column. Considering wavelength as the only variable, by comparing Fig. 3(a) and Fig. 3(d), Fig. 3(b) and Fig. 3(e), Fig. 3(c) and Fig. 3(f), we can see that larger wavelengths lead to larger leakage values. This is because we fixed the N.A. value in this study. Based on the formula $N.A = \frac{1}{\pi}\frac{\lambda}{\omega_0}$, where ω_0 is the focused beam size, with the same N.A. value, a larger wavelength laser results in a larger focused beam size. Therefore, cases in Figs. 3(d), 3(e), and 3(f) have a larger focused beam size than cases in Figs. 3(a), 3(b), and 3(c). With the same waterjet radius, a larger laser beam is likely to leak more.

For different N.A. values of 0.3325 (Fig. 4) and 0.1 (Fig. 5), similar conclusions can be drawn, i.e., for the same laser input (same N.A., and same wavelength), the laser beam is more likely to be fully confined inside the column with a larger waterjet diameter. When the waterjet diameter is smaller, some escaped light at the entrance of the waterjet can be seen; however, the laser intensity is stronger inside a smaller diameter waterjet where the laser is intensified due to total

Optics EXPRESS

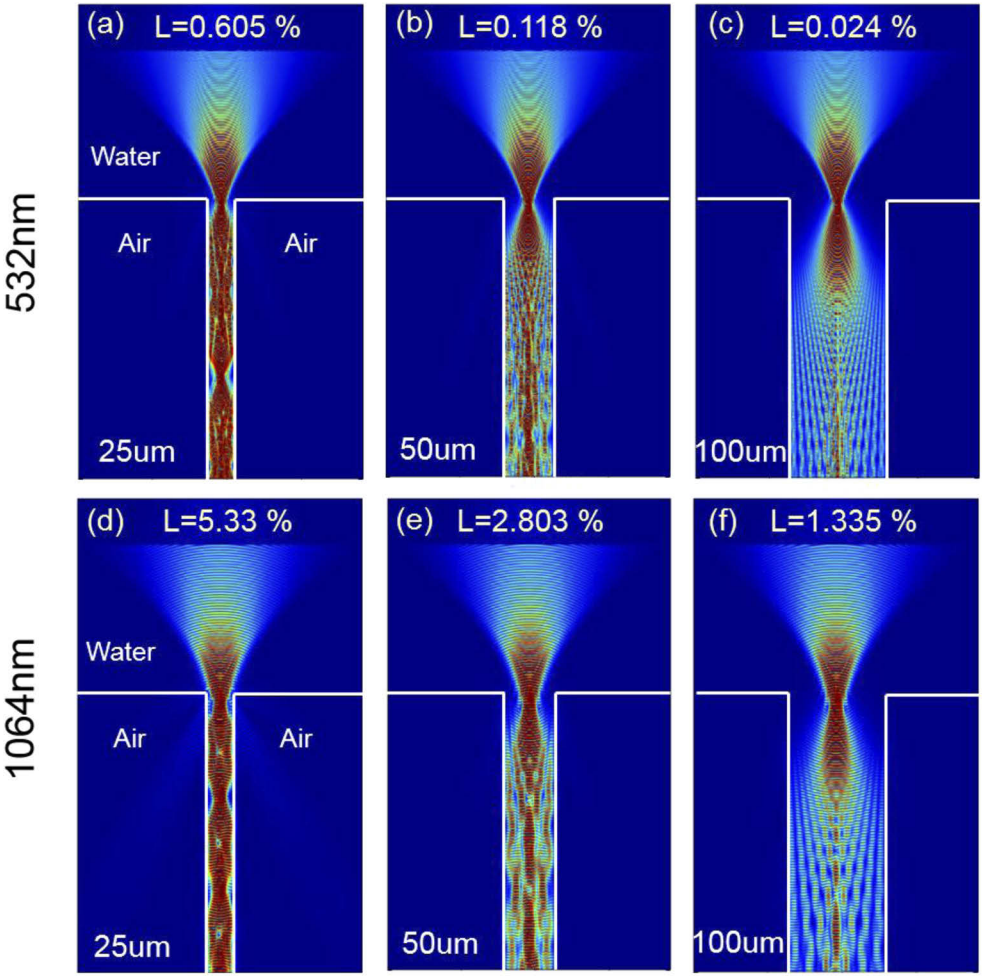

Fig. 3. Laser/waterjet coupling tests with N.A. = 0.6650. (a) 532 nm laser with R = 25 μm waterjet; (b) 532 nm laser with R = 50 μm waterjet; (c) 532 nm laser with R = 100 μm waterjet; (d) 1064 nm laser with R = 25 μm waterjet; (e) 1064 nm laser with R = 50 μm waterjet; (f) 1064 nm laser with R = 100 μm waterjet.

internal multi-reflection and interference. For the same N.A. values, different wavelengths result in different focused beam sizes. This also affects the coupling efficiency as a larger wavelength leads to a larger focused beam size. Hence, for the same waterjet diameter, leakage is more likely to occur for larger wavelength lasers, with the same N.A. value.

When the cases with different N.A. values (but having the same laser wavelength and the same waterjet diameter) are compared, the situation seems to be more complicated. For example, with the waterjet radius being 25 μm, in Fig. 3(a), Fig. 4(a), and Fig. 5(a), it is clearly shown that the leakage of laser light (L) decreases from 0.605% to 0.099%, and to 0.094% when the N.A. value varies from 0.6650 to 0.3325 and to 0.1000. The same conclusion can be drawn for the cases shown in Fig. 3(b), Fig. 4(b) and Fig. 5(b). But for other cases, this tendency seems to fail. For 1064 nm wavelength cases from Fig. 3(d), Fig. 4(d) and Fig. 5(d), (L) increases with the N.A. decreasing from 0.6650 to 0.3325 and finally to 0.1000, and for the rest of other cases there seems to be no tendency at all. And we believe that this might be caused by the combined effects of beam divergence angles for different N.A. cases and the waterjet entrance geometries.

Optics EXPRESS

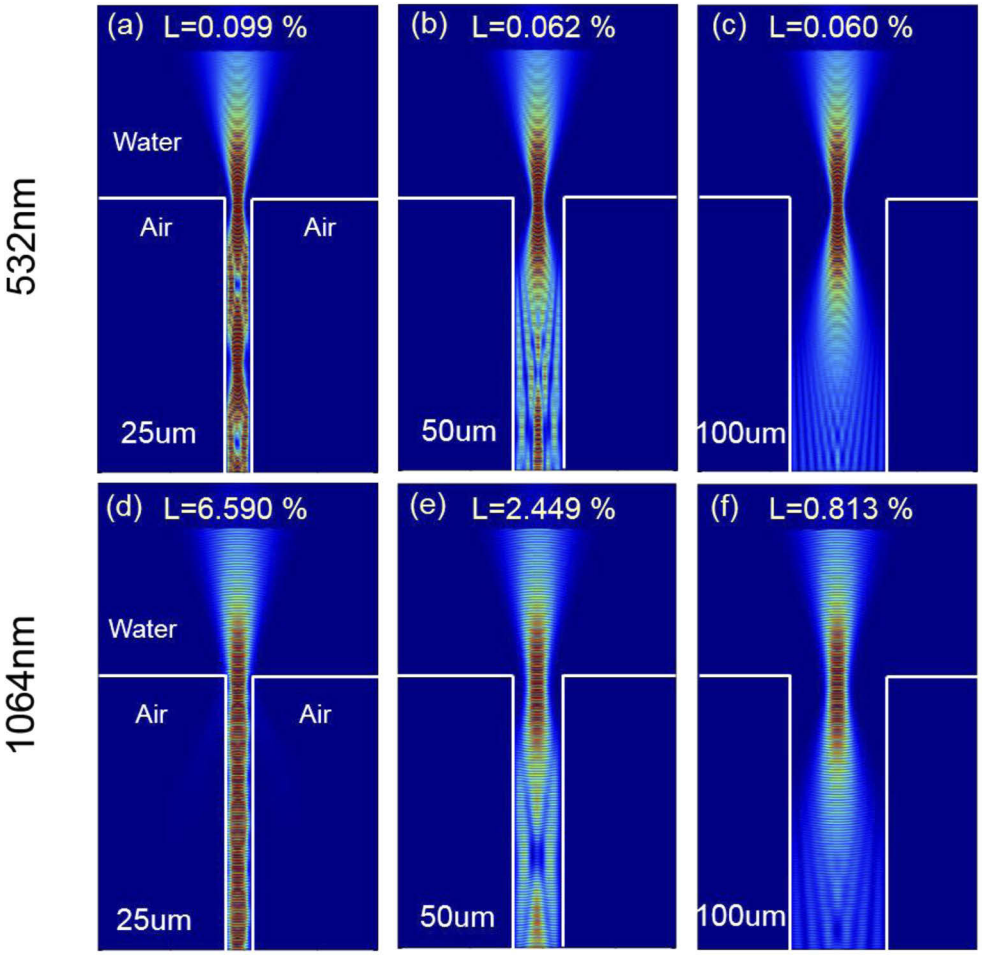

Fig. 4. Laser/waterjet coupling tests with N.A. = 0.3325. (a) 532 nm laser with R = 25 μm waterjet; (b) 532 nm laser with R = 50 μm waterjet; (c) 532 nm laser with R = 100 μm waterjet; (d) 1064 nm laser with R = 25 μm waterjet; (e) 1064 nm laser with R = 50 μm waterjet; (f) 1064 nm laser with R = 100 μm waterjet.

Also from $N.A. = \frac{1}{\pi}\frac{\lambda}{\omega_0}$, a higher N.A. value requires a smaller beam waist. Hence, for the same waterjet diameter, higher N.A. cases (those with smaller focused beam sizes) tend to be confined better within the waterjet columns without considering the divergence angle of the beam, reflection, and refraction. Taking them all into account, a larger N.A. results in a larger divergence angle of the laser beam, so that reflection and refraction at the entrance of the waterjet (both horizontal and vertical white lines) could be very complex and different for each case with a different N.A. value. And this could potentially contribute to a larger or smaller loss at the entrance. This combined effect makes it difficult to predict the loss for different N.A. values. But one conclusion can be drawn from Fig. 3, Fig. 4, and Fig. 5 that the relative size of the focused laser beam as compared to the waterjet diameter plays the most important role in determining energy leakage for laser/waterjet coupling. To achieve higher laser/waterjet coupling efficiencies, the focused laser beam diameter should be smaller than the waterjet column diameter. If the waterjet column diameter is much larger than the focused laser beam (such as the 100 μm cases shown in Fig. 3, Fig. 4, and Fig. 5), the loss will be very small. However, for those cases, internal

Optics EXPRESS

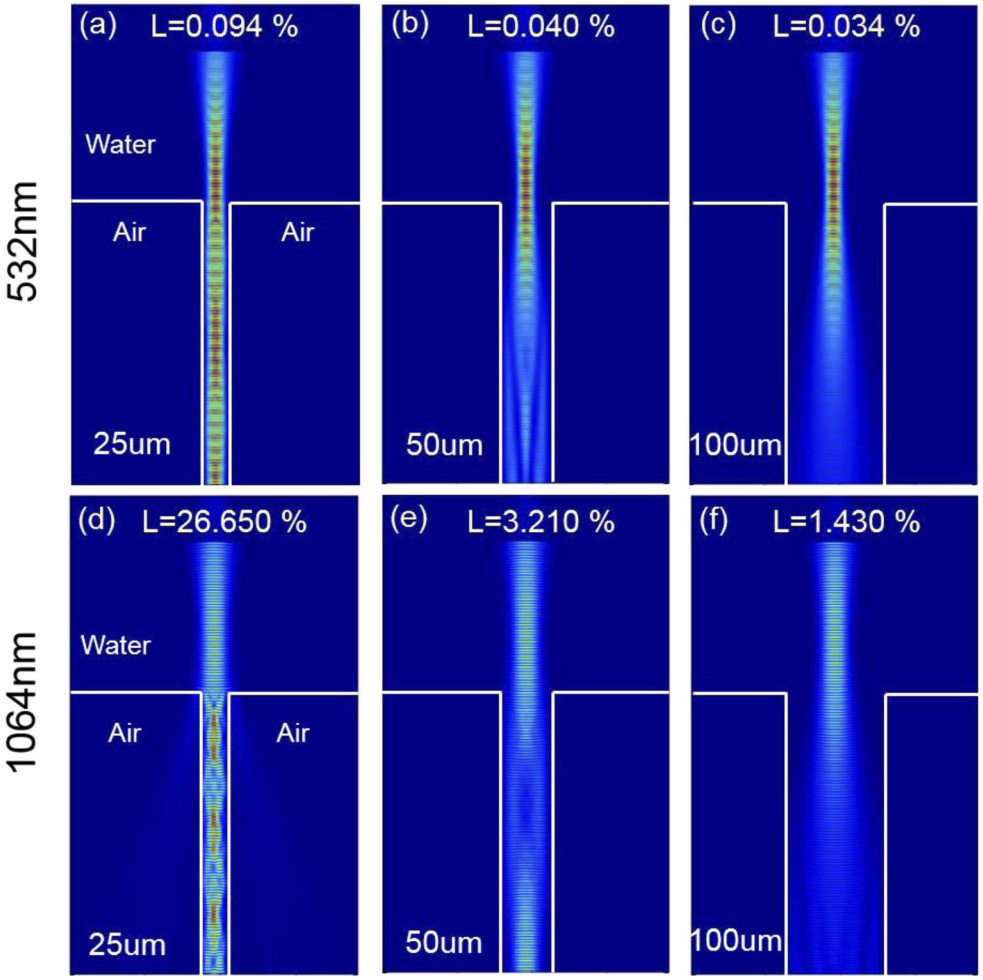

Fig. 5. Laser/waterjet coupling tests with N.A. = 0.1000. (a) 532 nm laser with R = 25 μm waterjet; (b) 532 nm laser with R = 50 μm waterjet; (c) 532 nm laser with R = 100 μm waterjet; (d) 1064 nm laser with R = 25 μm waterjet; (e) 1064 nm laser with R = 50 μm waterjet; (f) 1064 nm laser with R = 100 μm waterjet.

reflections and interferences are not as strong as they are for waterjets with smaller diameters. This could potentially affect the fabrication quality as the energy might not be intense enough, and the intensity distributions might not be uniform enough, at the target material surface. To ensure better manufacturing quality, it is the authors' opinion that the focused beam size should be slightly smaller than the waterjet diameter to ensure an intensified energy output that is uniformly distributed.

For the investigation of the laser beam absorption behavior of the waterjet-guided laser processing, two commonly used laser wavelengths, a cost-effective industry-preferred IR laser of 1064 nm wavelength and its second harmonic of 532 nm green light laser, were chosen as the energy sources to perform a comparison. For water at room temperature as the working medium, the 532 nm laser is known to have a much higher transmission value and the 1064 nm laser has a higher absorption due to their different optical properties.

Optics EXPRESS

Apart from the wavelength differences, the geometries of the waterjet columns could also affect the propagation of the laser beam. In this study, we considered several different waterjet shapes including the ideal cylindrical column and water columns with different periodic displacement sinusoids and different amplitudes, as shown in Figs. 6(b)–6(e). Figure 6(b) shows a perfectly cylindrical water column with a uniform radius and a length of 2 cm; Fig. 6(c) shows a waterjet with a wavy outer surface that fluctuates as a sinusoidal function within one period. The amplitude A of the waterjet is assumed to be only 5 μm. Figure 6(d) is similar to Fig. 6(b), but the amplitude of this case was set to 15 μm. Finally, Fig. 6(e) has 3 sinusoidal periods within the length and the amplitude was set to 15 μm. All simulations were conducted in three-dimensions, and the geometries shown here in Fig. 6 are the symmetric planes of each case crossing the central axis line. One thing to note here is that the aspect ratio of the computational domain (at the symmetric plane) was roughly 150 μm : 20000 μm = 0.0075, therefore it was too difficult to show all the detailed information due to the extreme length of the waterjet dimension. Therefore, we manually increased the width by a factor of 20 for better illustration without changing the actual results.

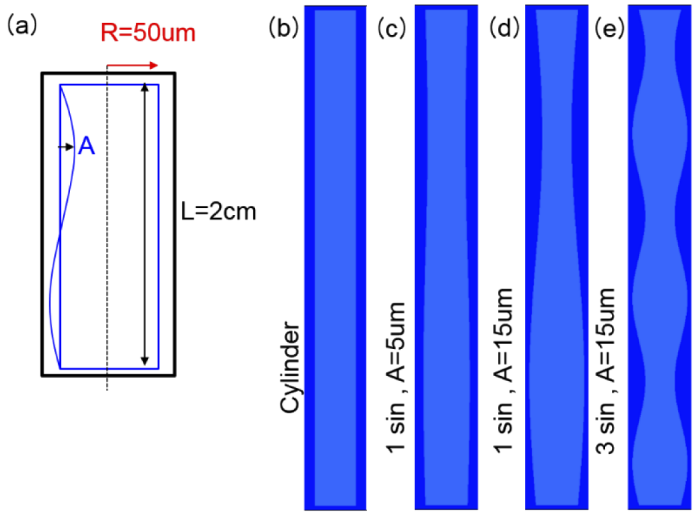

Fig. 6. Various waterjet column shapes for FDTD simulations. (a). schematic of the waterjet geometry; (b) cylindrically shaped waterjet; (c) waterjet with a single sinusoidal displacement on the outer surface and an amplitude of 5 μm; (d) waterjet with a single sinusoidal displacement on the outer surface and an amplitude of 15 μm; (d) waterjet with 3 sinusoidal displacements on the outer surface and an amplitude of 15 μm.

Figure 7 shows the overall laser propagation patterns inside the waterjet columns, arranged in terms of laser wavelengths and waterjet geometries. Computations were performed in 3D, but each figure here [Figs. 7(a)–7(h)] only shows the electric field on the symmetric plane where the laser beam passes through the axis of the waterjet. The Gaussian beam is focused and irradiated from the top of the waterjet (through a nozzle, not shown here) vertically and undergoes reflections and interferences, as clearly shown in Fig. 7.

Comparing the results between the laser wavelength of 532 nm [Figs. 7(a)–7(d)] and the wavelength of 1064 nm [Figs. 7(e)–7(h)], several big differences can be seen regarding the laser beam propagation patterns within the waterjets. It is clearly shown that the electric field of the 532 nm laser beam propagating inside the waterjets almost remains constant from top to bottom for the whole length of the waterjet. The transmission value T of each case is also listed in Figs. 7(a)–7(d), and they are 0.9112, 0.9100, and 0.8981 [from Figs. 7(a) to 7(d)]. The transmission values are almost the same for all cases with very small variations, and when the fluctuation of the waterjet

Optics EXPRESS

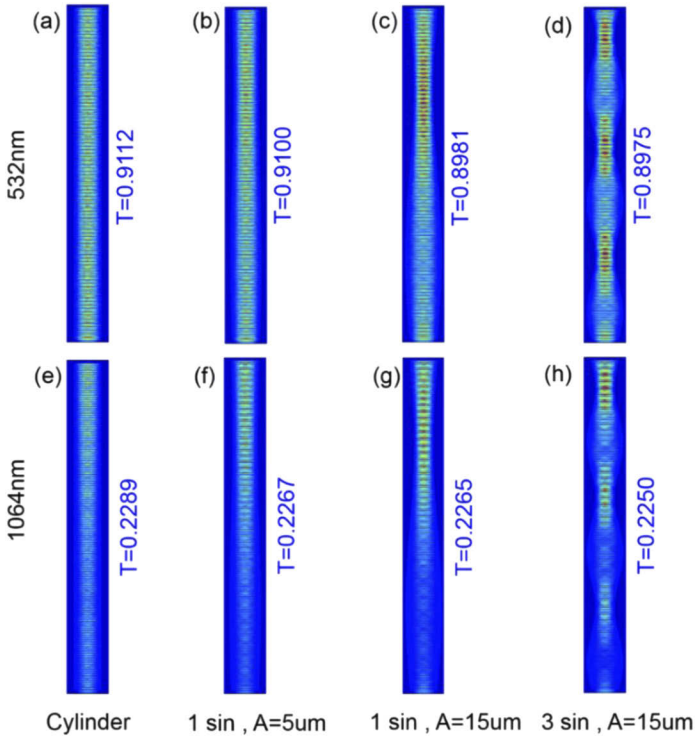

Fig. 7. 1064 nm and 532 nm laser propagation within various waterjet surface geometries. (top) 532 nm laser beam (bottom) 1064 nm laser beam (left to right) a perfect cylindrically shaped waterjet, a waterjet with a single sinusoidal displacement on the outer surface and an amplitude of 5 um, a waterjet with a single sinusoidal displacement on the outer surface and an amplitude of 15 um and a waterjet with 3 sinusoidal displacements on the outer surface and an amplitude of 15 um, respectively.

gets stronger (e.g., larger amplitude or smaller periods), the transmission seems to become lesser. Similar conclusions can be drawn for the 1060 nm cases as well. Apparently, water has a much larger absorption value for the 1060 nm laser as the electrical field becomes much dimmer when the laser beam approaches the bottom of the waterjet, as expected. Despite the energy loss, a similar tendency for transmission is noticed. For all 4 cases, transmission values are 0.2289, 0.2267, 0.2265, and 0.2250 [from Figs. 7(e) to 7(h)], and T decreases when the fluctuation level increases. From these simulations, we can learn that the transmission of a laser beam decreases as the waterjet fluctuation level increases, and this is understandable because sustaining a stable air-water interface requires extra energy. It is noteworthy that, in the extreme case where the liquid column breaks up into water droplets, the laser beam cannot be guided, resulting in T = 0%. Despite the decrease in transmission values when the fluctuation level increases, however, the actual difference is small among those cases as long as the waterjet is still continuous.

Apart from the laser propagation patterns with waterjets, the Joule heating for each case has also been calculated. The results are shown in Fig. 8. Joule heating patterns are shown in the same arrangements as the electrical field patterns inside the waterjet columns on the same symmetrical planes and their respective absorption values (A=1-T) are presented in Fig. 8. Because Joule heating is a function of the electrical field **E**, Joule heating patterns closely resemble the laser propagation patterns (electrical fields). Based on the different geometries of the waterjet, the electrical field is confined and compressed (via internal reflection and interference) within the

Optics EXPRESS

columns. When the laser reaches the pinched area (smaller column diameter), the electric field is concentrated and becomes stronger, resulting an intensified Joule heating effect. On the other hand, when the laser reaches the bulging section of the waterjet, the electric field expands and becomes weaker; therefore, the Joule heating effect also becomes weaker. This phenomenon can be clearly seen in Figs. 8(c), 8(d) and 8(g), 8(h), where dark-red areas indicate intensified Joule heating sections while light blue areas indicate weak Joule heating sections. When the intensified laser reaches the workpiece, the laser ablates the material by melting and vaporization; hence, the Joule heating patterns at the workpiece surface directly affect the quality of the cuts. Intensified and uniform Joule heating patterns are more desirable. This calls for more stable waterjets (without much fluctuation). One notable point here is that the Joule heating patterns for 532 nm should be much lower than the ones for 1064 nm with the same laser energy input. If the same scale bar is adopted and the maximum value of J_h for 1064 nm is used as reference, the patterns for 1064 nm will be exactly the same as the ones shown in Figs. 8(e)–8(h). However, the patterns for 532 nm will be much dimmer and can be barely seen. Therefore, in Figs. 8(a)–8(d) for 532 nm wavelength cases, a smaller reference is chosen in order to show all the details.

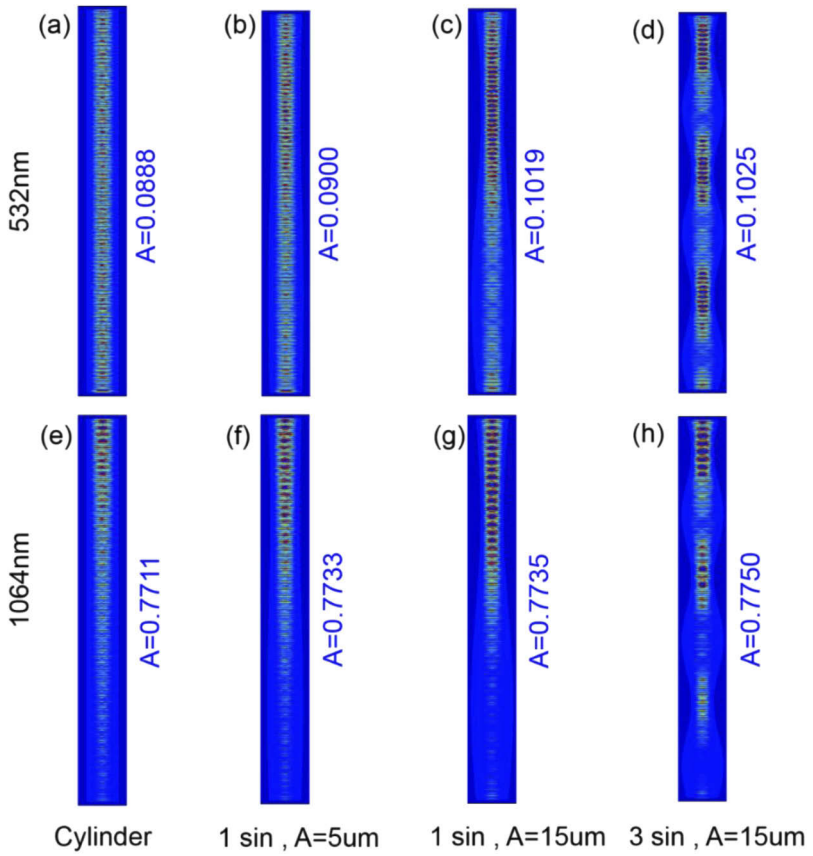

Fig. 8. Joule heating patterns of 1064 nm and 532 nm laser propagation within various waterjet geometries. (top) 532 nm laser beam (bottom) 1064 nm laser beam (left to right) a perfect cylindrically shaped waterjet, a waterjet with a single sinusoidal displacement on the outer surface and an amplitude of 5 um, a waterjet with a single sinusoidal displacement on the outer surface and an amplitude of 15 um and a waterjet with 3 sinusoidal displacements on the outer surface and an amplitude of 15 um, respectively.

Optics EXPRESS

In this study, temperature distributions due to the Joule heating were also calculated for the Joule heating patterns obtained with N.A. = 0.3325 (Fig. 4) inside 2 cm long perfect cylindrical waterjets with diameters of 25 and 50 μm. Figure 9 and Fig. 10 show the steady-state results of 532 nm and 1064 nm wavelength lasers, where the top and bottom figures are the results for the waterjet radius of R = 25 μm and R = 50 μm, respectively. The waterjet columns were intentionally widened by a factor of 10 in the lateral direction for better illustration. Note that each figure has a different range of scale bars. In these figures, the black solid lines are 100°C contour lines, where the vaporization begins. As seen from the figures, higher temperatures are observed in the results of the smaller waterjet radius due to concentrated electric fields. In Fig. 9, where the waterjet velocity is very small ($U = 0.1$ m/s), the maximum temperature is over 100°C, and the evaporation that causes instabilities of the waterjet may occur. As the waterjet velocity increases, convection takes away more heat and leads to temperature drops. If the water flows very rapidly ($U = 50$ m/s), the temperature hardly changes. Therefore, in the case of a 532 nm wavelength laser, the proper temperature field can be easily obtained. Compared to the results of a 532 nm wavelength laser, the results of the 1064 nm wavelength laser show much higher temperature distributions owing to the increased heating effect. In this case, evaporation still occurs even for a very rapid flow. Thus, for the 1064 nm wavelength laser, a much higher waterjet velocity is necessary, and the processing is not practical.

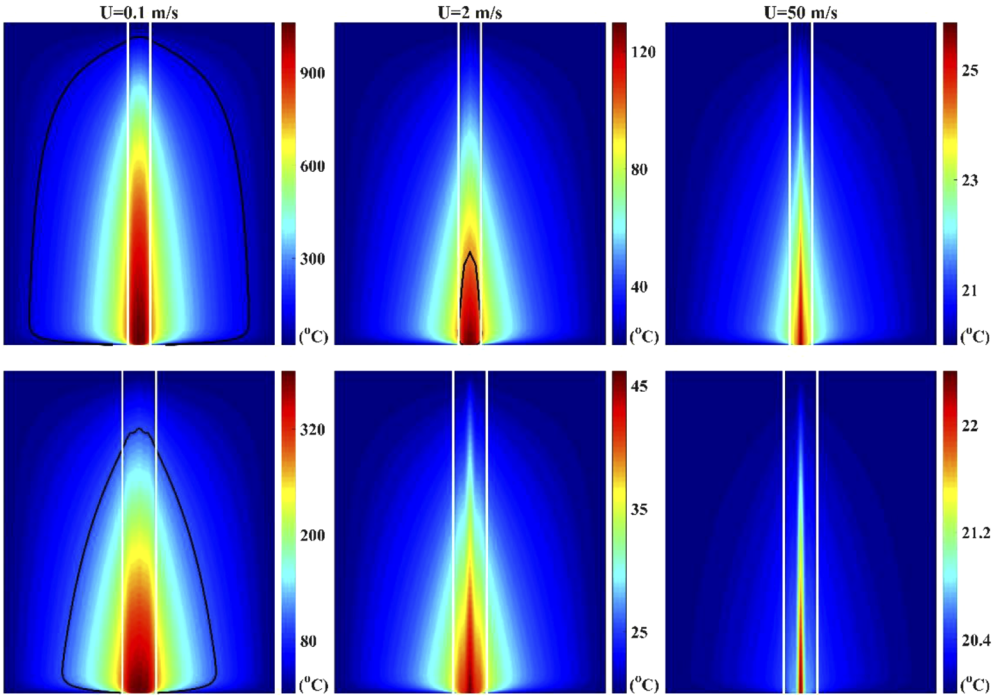

Fig. 9. Temperature distributions of 532 nm wavelength laser for three different waterjet speeds. (White lines represent the waterjet column) (Top figures) steady state results for the waterjet radius of 25 μm. (Bottom figures) steady state results for the waterjet radius of 50 μm.

The quality of the waterjet-guided laser processing is also affected by the Plateau-Rayleigh instability. If the waterjet stream breaks up due to the waterjet instability, this waterjet-guided processing is impossible. Therefore, for reliable and stable material processing, a longer break-up length is required. The break-up length depends on the Reynolds number (Re), Ohnesorge

Optics EXPRESS

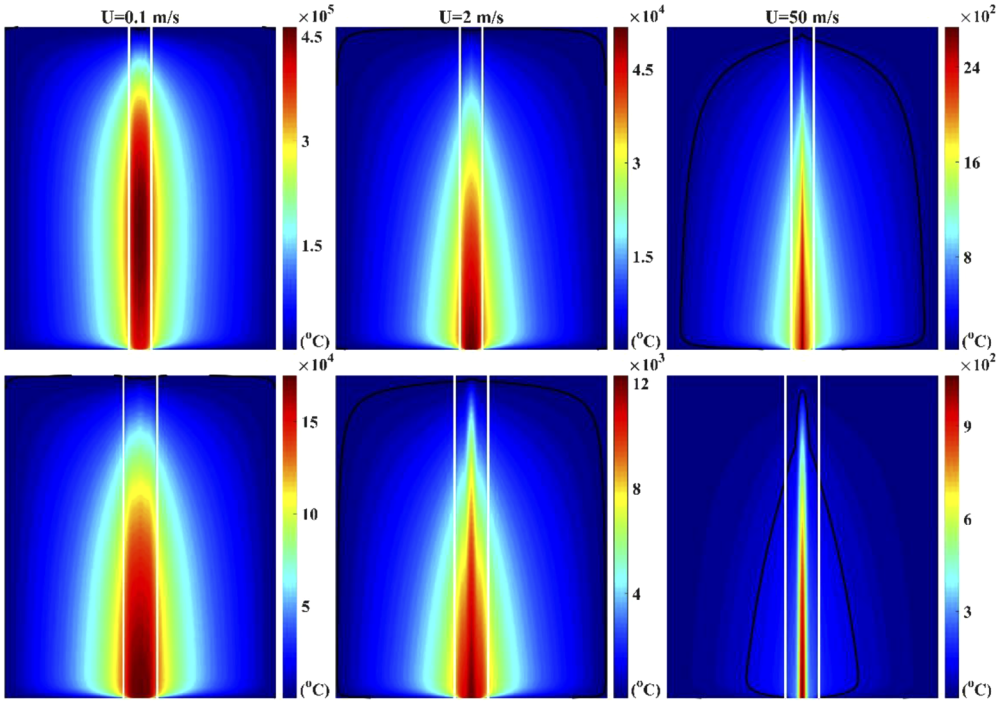

Fig. 10. Temperature distributions of 1064 nm wavelength laser for three different waterjet speeds. (White lines represent the waterjet column) (Top figures) steady state results for the waterjet radius of 25 μm. (Bottom figures) steady state results for the waterjet radius of 50 μm.

number (Oh), and also other factors [25] as follows:

$$\mathrm{Re} = \frac{\rho U D}{\mu}, \quad \mathrm{Oh} = \frac{\mu}{\sqrt{\rho \sigma D}}, \tag{11}$$

where μ is the viscosity, σ is the surface tension, and D is the jet diameter. In the above problems, the ranges of Reynolds and Ohnesorge numbers are 5–5000 and 0.0117–0.0165. According to the experimental results in [25], in this range of dimensionless numbers, the break-up length increases almost linearly as velocity increases. Thus, the increase in the waterjet velocity is desirable for the quality, however, there is a cost increase to maintain a high pressure at inlet.

In summary, a 532 nm laser has a larger transmission over a 1064 nm laser owing to the smaller absorption in the water medium. When the N.A. and wavelength value are fixed, the transmission efficiency increases with the increase of the waterjet diameter, as the laser beams are more likely to be confined within the larger waterjets. Meanwhile, a smaller waterjet diameter delivers much stronger and more uniformly distributed electric fields due to the multireflection and interference. For the cases with the same wavelength but different N.A. values, the tendency of the transmission efficiency seems to be very difficult to be determined as the divergence angle now plays a huge role at the entrance (both horizontal and vertical interfaces) of the waterjet. However, the differences for different N.A. cases are very minor for the wavelength of 532 nm while the difference is much significant for 1064 nm. This is another reason for the 1064 nm laser being not a good candidate for waterjet guided cutting. The waviness of the waterjet outer surface also plays a role in delivering the laser energy to the work piece. The transmission efficiency decreases with the increase of the waviness of the waterjet outer surface, but it seems the impact

Optics EXPRESS

on the energy delivery efficiency is significantly minor as long as the waterjet is continuous and don't break into droplets. The increases in the waterjet velocity lowers the temperature and increases the break-up length. Thus, the material processing becomes stable.

4. Conclusions

We have studied laser beam propagation in waterjet-guided laser processing using a multiphysics numerical approach combining the Maxwell equations and the heat equation. The major findings are summarized as follows.

- The 532 nm green laser has a much larger transmission (~90% for a 2 cm long waterjet) compared to the 1064 nm IR laser (~20% for a 2 cm long waterjet) as expected.
- Relative size of the focused beam compared to the waterjet diameter plays a vital role in the laser/waterjet coupling efficiency. The authors believe that the focused beam size should be slightly smaller than the waterjet diameter to ensure an intensified energy output that is uniformly distributed.
- The effect of different N.A values for the same laser wavelength seems to be very complicated to predict, considering the different divergence angles of each case and the laser propagation (reflection/refraction/interference) at both horizontal and vertical interfaces at the waterjet entrance.
- Despite the overall transmission values decreasing with the increase of the fluctuation level of waterjets, the actual difference is very minor amongst different cases as long as the waterjet remains continuous.
- When the laser reaches the pinched area (smaller column diameter), the electric field is concentrated and becomes stronger, resulting an intensified Joule heating effect. On the other hand, when the laser reaches the bulging section of the waterjet, the electric field expands and becomes weaker, and the Joule heating effect also becomes weaker.
- From the heat transfer viewpoint, the 532 nm wavelength laser is more suitable for the waterjet-guided laser processing than the 1064 nm wavelength laser because the evaporation of water could be readily prevented owing to the much smaller absorption coefficient at 532 nm. Under the conditions used for the thermal analysis, the increase in the waterjet velocity improved the quality of the processing.

Funding

National Research Foundation of Korea (NRF-2019R1A2C2089114).

Disclosures

The authors declare no conflicts of interest.

References

1. J. D. Koralek, J. B. Kim, P. Bruza, C. B. Curry, Z. J. Chen, H. A. Bechtel, A. A. Cordones, P. Sperling, S. Toleikis, J. F. Kern, S. P. Moeller, S. H. Glenzer, and D. P. DePonte, "Generation and characterization of ultrathin free-flowing liquid sheets (vol 9, 2018)," Nat. Commun. **9**(1), 1353 (2018).
2. C. A. A. Rashed, L. Romoli, F. Tantussi, F. Fuso, M. Burgener, G. Cusanelli, M. Allegrini, and G. Dini, "Water jet guided laser as an alternative to EDM for micro-drilling of fuel injector nozzles: A comparison of machined surfaces," J. Manuf. Process. **15**(4), 524–532 (2013).
3. G. Y. Zhang, Z. Zhang, Y. F. Wang, C. H. Guo, and W. W. Zhang, "Gas shrinking laminar flow for robust high-power waterjet laser processing technology," Opt. Express **27**(26), 38635–38644 (2019).

Optics EXPRESS

4. R. Zahoor, G. Belsak, S. Bajt, and B. Sarler, "Simulation of liquid micro-jet in free expanding high-speed co-flowing gas streams," Microfluid. Nanofluid. **22**(8), 87 (2018).
5. J. A. Porter, Y. A. Louhisalmi, J. A. Karjalainen, and S. Fuger, "Cutting thin sheet metal with a water jet guided laser using various cutting distances, feed speeds and angles of incidence," Int. J. Adv. Manuf. Technol. **33**(9-10), 961–967 (2007).
6. Y. K. Madhukar, S. Mullick, and A. K. Nath, "Development of a water-jet assisted laser paint removal process," Appl. Surf. Sci. **286**, 192–205 (2013).
7. Y. Shi, Z. L. Jiang, J. Cao, and K. F. Ehmann, "Texturing of metallic surfaces for superhydrophobicity by water jet guided laser micro-machining," Appl. Surf. Sci. **500**, 144286 (2020).
8. A. Lister, "Entwicklung Und Konstruktion Von Entschwefelungs-Reaktoren," Chem-Ing-Tech **37**, 67 (1965).
9. B. Richerzhagen, "Chip singulation process with a water jet-guided laser," Solid State Technol. **44**, S25–S28 (2001).
10. C. F. Li, D. B. Johnson, and R. Kovacevic, "Modeling of waterjet guided laser grooving of silicon," Int. J. Adv. Manuf. Technol. **43**(9), 925–936 (2003).
11. D. Kray, S. Hopman, A. Spiegel, B. Richerzhagen, and G. P. Willeke, "Study on the edge isolation of industrial silicon solar cells with waterjet-guided laser," Sol. Energy Mater. Sol. Cells **91**(17), 1638–1644 (2007).
12. S. Marimuthu, J. Dunleavey, Y. Liu, B. Smith, A. Kiely, and M. Antar, "Water-jet guided laser drilling of SiC reinforced aluminium metal matrix composites," J. Compos. Mater. **53**(26-27), 3787–3796 (2019).
13. D. Sun, F. Z. Han, and W. S. Ying, "The experimental investigation of water jet-guided laser cutting of CFRP," Int. J. Adv. Manuf. Technol. **102**(1-4), 719–729 (2019).
14. C. Deng and H. Ki, "FDTD method for laser absorption in metals for large scale problems," Opt. Express **21**(21), 25467–25479 (2013).
15. A. Taflove and S. C. Hagness, *Computational Electrodynamics: The Finite-Difference Time-Domain Method*, 3rd ed. (Artech House, 2005).
16. C. Deng, J. Kim, S. Oh, and H. Ki, "Electrodynamic simulation of energy absorption in laser keyhole welding of zinc-coated and uncoated steel sheets," J. Mater. Process. Technol. **231**, 412–421 (2016).
17. C. Deng and H. Ki, "Finite-difference time-domain simulation of laser beam absorption in fully penetrated keyholes," J. Appl. Phys. **114**(16), 164901 (2013).
18. J. Kim and H. Ki, "355, 532, and 1064 nm picosecond laser interaction with grass tissues," J. Appl. Phys. **112**(11), 114908 (2012).
19. J. Kim and H. Ki, "CO2 and Er:YAG laser interaction with grass tissues," J. Appl. Phys. **113**(4), 044902 (2013).
20. M. H. Niemz, *Laser-Tissue Interactions: Fundamentals and Applications*, 3rd, enlarged ed. (Springer-Verlag, 2004).
21. D. Lukas, N. Pan, A. Sarkar, M. Weng, J. Chaloupek, E. Kostakova, L. Ocheretna, P. Mikes, M. Pociute, and E. Amler, "Auto-model based computer simulation of Plateau-Rayleigh instability of mixtures of immiscible liquids," Phys. A **389**(11), 2164–2176 (2010).
22. R. Mead-Hunter, A. J. C. King, and B. J. Mullins, "Plateau Rayleigh Instability Simulation," Langmuir **28**(17), 6731–6735 (2012).
23. I. Ahmed, E. H. Khoo, and E. P. Li, "Development of the CPML for Three-Dimensional Unconditionally Stable LOD-FDTD Method," IEEE Trans. Antennas Propag. **58**(3), 832–837 (2010).
24. D. Perrottet, C. Boillat, S. Amorosi, and B. Richerzhagen, "PV processing: Improved PV-cell scribing using water jet guided laser," Refocus **6**(3), 36–37 (2005).
25. M. Etzold, A. Deswal, L. Chen, and F. Durst, "Break-up length of liquid jets produced by short nozzles," Int. J. Multiphase Flow **99**, 397–407 (2018).